





# Evidence for a different dispersion of the topological edge state of germanene at armchair and zigzag edges

Harold J. W. Zandvliet , Dennis J. Klaassen , and Pantelis Bampoulis 

*Physics of Interfaces and Nanomaterials, MESA+ Institute, University of Twente, P.O. Box 217, 7500AE Enschede, The Netherlands*

 (Received 8 January 2024; revised 20 February 2024; accepted 28 February 2024; published 14 March 2024)

Utilizing a tunneling spectroscopy approach based on the energy-dependent inverse decay length, our research unveils distinct dispersion characteristics of germanene's topological edge states. We observe a pronounced variance in Fermi velocity, with armchair edges exhibiting a velocity higher than zigzag edges by about an order of magnitude. This difference highlights the influence of edge termination on the energy-momentum dispersion relation of one-dimensional topological edge states in two-dimensional topological insulators, aligning with the theoretical framework of a Kane-Mele topological insulator.

DOI: [10.1103/PhysRevB.109.115419](https://doi.org/10.1103/PhysRevB.109.115419)

## I. INTRODUCTION

Two-dimensional topological insulators are materials that exhibit the quantum spin Hall (QSH) effect [1–5]. They are characterized by a gapped interior and topologically protected helical edge states. The electronic transport in these edge states is predicted to be dissipationless because backscattering is forbidden due to spin-momentum locking and time reversal symmetry [6–9]. The latter offers great possibilities for energy-efficient quantum devices, such as topological field-effect transistors, interconnects, and topological (qu)bits [10–14]. Topological edge states have been observed in band-inverted semiconductors and two-dimensional materials [5,15–22], such as bismuthene [23] and germanene [24]. To exploit the unique characteristics of topologically protected edge states it is of utmost importance to study the properties of these states, particularly in the vicinity of the Fermi level. Among the most important quantities is the Fermi velocity of the electrons. Unfortunately, the conventional methods to measure the Fermi velocity of electrons, i.e., angle-resolved photoemission [25] and quasiparticle interference [26], cannot be applied to topologically protected edge states. Angle-resolved photoemission is not applicable owing to its macroscopic averaging, whereas the absence of backscattering in topologically protected edge states disqualifies quasiparticle interference.

Here we propose a method to measure the energy-momentum dispersion of topological edge states. The method relies on the energy dependence of the inverse decay length in a scanning tunneling microscopy tunnel barrier and is only applicable when there is only one energy band in the energy window of interest. Our material of choice is germanene [27–33]; germanene is the germanium analog to graphene. We recently demonstrated that germanene is a two-dimensional topological insulator that hosts a topological edge state [24]. In this study, we will determine the Fermi velocity of this topological edge state for two different edge terminations—the zigzag and armchair edge.

## II. EXPERIMENTAL METHODS

The scanning tunneling microscopy and spectroscopy measurements are performed with an ultrahigh vacuum low-temperature Omicron scanning tunneling microscope. The background pressure in the ultrahigh vacuum system is lower than  $3 \times 10^{-11}$  mbar. Germanene layers are produced by depositing a few monolayers of Pt on an atomically clean Ge(110) substrate. After Pt deposition, the Ge(110) substrate is annealed at a temperature of about 1100 K for several minutes. At this temperature  $\mu\text{m}$ -sized eutectic  $\text{Ge}_{0.78}\text{Pt}_{0.22}$  droplets form on the Ge(110) substrate. Upon cooling down the eutectic phase undergoes spinodal decomposition into a pure Ge phase and a  $\text{Ge}_2\text{Pt}$  alloy [27,34–37]. As discussed extensively in Refs. [24,27] the  $\text{Ge}_2\text{Pt}$  clusters are decorated with several germanene layers. The germanene layers exhibit a buckled honeycomb structure, where one of the hexagonal sublattices is displaced in a direction normal to the germanene sheet with respect to the other hexagonal sublattice. The first germanene layer, often referred to as the buffer layer, couples to the underlying  $\text{Ge}_2\text{Pt}(101)$  substrate and does not exhibit the properties of a two-dimensional topological insulator. The other germanene layers are two-dimensional topological insulators that host a topologically protected helical edge state [24]. The differential conductivity,  $\frac{dI}{dV}$ , spectra are measured at 77 K using a lock-in amplifier. The frequency of the lock-in amplifier was set to 1.1–1.2 kHz and the modulation voltage was 20 mV.

## III. RESULTS AND DISCUSSION

Figure 1(a) shows a scanning tunneling microscopy image of few layer germanene on  $\text{Ge}_2\text{Pt}(101)$ . A germanene buffer layer is present in the lower right of the image, whereas one-layer (1L) and two-layer (2L) germanene on the buffer layer are found at the lower left and upper left of the image, respectively. Figure 1(b) shows a simple schematic cartoon of the germanene/buffer layer/ $\text{Ge}_2\text{Pt}$  system. A scan taken

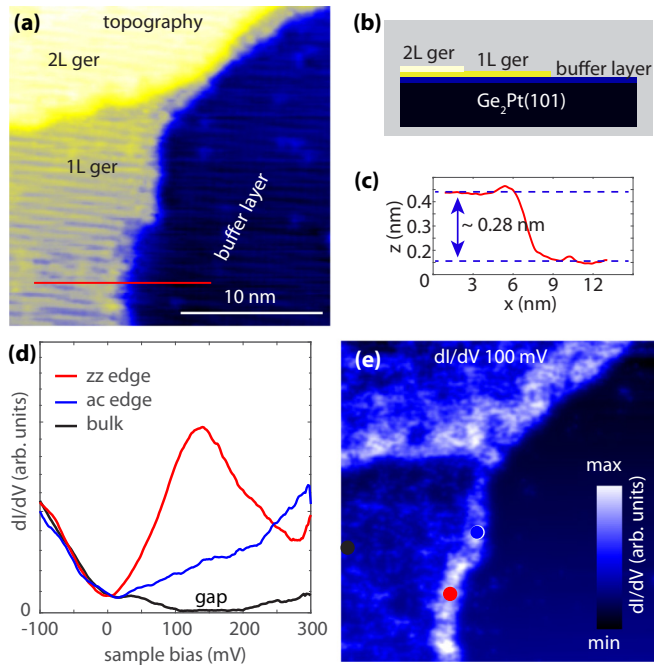


FIG. 1. (a) Scanning tunneling microscopy image of germanene on  $\text{Ge}_2\text{Pt}$ . Buffer layer, 1L (one germanene layer on a buffer layer/ $\text{Ge}_2\text{Pt}$ ) and 2L (two germanene layers on a buffer layer/ $\text{Ge}_2\text{Pt}$ ) regions are shown. (b) Schematic diagram of the system. (c) Line scan shown by the red line in panel (a) taken across a single layer high step edge. (d)  $dI/dV$  versus  $V$  for bulk (black curve), armchair edge (blue), and zigzag edge (red). Set-point sample bias  $-0.3$  V and set-point tunnel current  $0.3$  nA. (e) Map of the differential conductivity ( $dI/dV$ ) at a sample bias ( $V$ ) of  $100$  mV.

across the red line in Fig. 1(a) is displayed in Fig. 1(c). The height of the step edge is  $0.28$  nm, which corresponds to the height of a single germanene layer [24,27]. Figure 1(d) displays the differential conductivity versus sample bias of the interior of germanene (black curve), an armchair terminated edge (blue curve), and a zigzag terminated edge (red curve). In the interior of germanene a band gap with a width of about  $100$ – $150$  meV is observed. The armchair and zigzag edges have a nonzero density of states filling the bulk band gap region, hinting at the presence of a metallic edge state. The density of states of the edges in the middle of the band gap is, however, substantially higher for the zigzag edge than the armchair edge. We will discuss this salient difference in more detail below. Figure 1(e) shows a differential conductivity ( $dI/dV$ ) map of the scanning tunneling microscopy image displayed in Fig. 1(a). The ( $dI/dV$ ) map is taken near the maximum of the  $dI/dV$  peak at  $100$  mV; see Fig. 1(d).

An atomic resolution scanning tunneling microscopy image of the germanene edge is shown in Fig. 2(a). Given the challenge of discerning atomic details at the edge, we have fast Fourier transform (FFT) filtered the image shown in Fig. 2(a); see Fig. 2(b). The edge at positions 1–8 has a zigzag termination, whereas positions 9–15 correspond to an armchair edge termination. The differential conductivity as a function of sample bias at locations 1–15 and the interior of the material (bulk) are displayed in Fig. 2(c). It is immediately clear that the zigzag terminated edge exhibits a

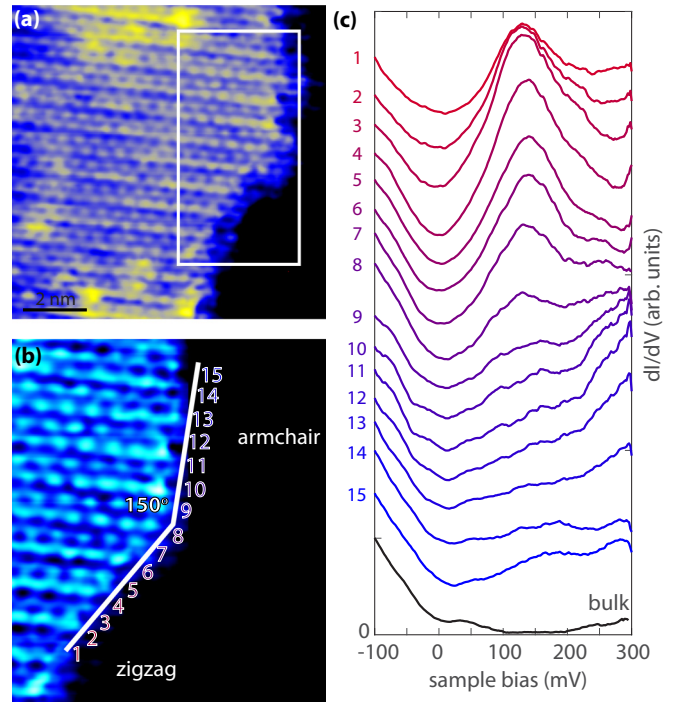


FIG. 2. (a) Scanning tunneling image of germanene showing an edge. (b) Filtered version of panel (a) showing zigzag and armchair terminated parts of the edge. The edge positions are labeled from 1 to 15. (c)  $dI/dV$  taken at different locations of the edge labeled from 1 to 15; see panel (b). For clarity the curves 1–15 are shifted in the  $y$  direction. The black curve, curve 4, and curve 12 correspond to the black curve, the red curve, and the blue curve shown in Fig. 1(d), respectively. Set-point sample bias  $-0.3$  V and set-point tunnel current  $0.3$  nA. A figure where all  $dI/dV$  curves, shown in panel (c), are plotted without offset can be found in the Supplemental Material (Fig. S3).

strong and well-defined peak, which is located in the middle of the bulk band gap, whereas the density of states of the armchair terminated edge positions is much lower. It should be noted that the strength of the edge state at the zigzag edge decreases near the kink sites, located at positions 1 and 8, respectively. In addition, at location 8 the peak of the edge state exhibits a shape that is somewhere in between a zigzag and armchair state. These observations can be explained by the averaging effect in scanning tunneling microscopy and spectroscopy, which is caused by the finite radius of curvature of the scanning tunneling microscopy tip. For completion, we provide a  $dI(V)/dV$  curve recorded at a straight zigzag edge in Fig. S1 of the Supplemental Material [38].

To explain our scanning tunneling spectroscopy observations we will first briefly elaborate on the density of states of a topologically protected edge state. The topologically protected helical edge state of germanene is one-dimensional and the dispersion relation is assumed to be linear ( $E - E_D = \pm \hbar v_F |k|$ ) (see the Supplemental Material [38]). The helical edge state is located in the topological gap of germanene. Please note that the gap at the  $\Gamma$  point of germanene is larger than the topological gap at the  $K$  and  $K'$  points [24]. Under the aforementioned assumptions, the density of states in energy

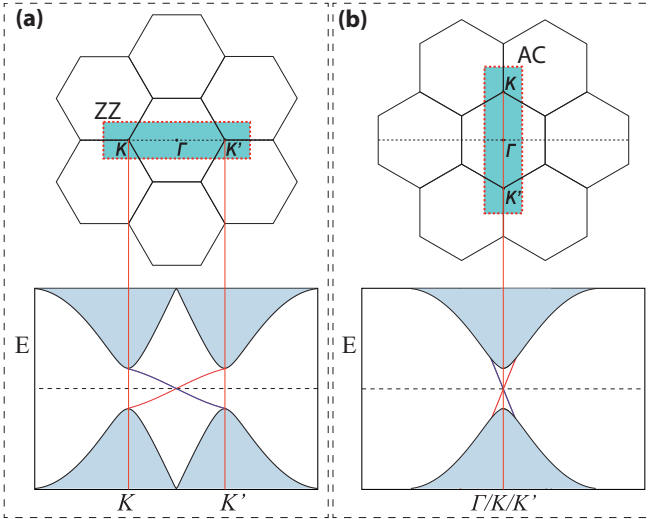


FIG. 3. Reciprocal lattice of germanene (top panels) and electronic band structure of (a) a zigzag and (b) an armchair edge (bottom panels).

space is given by

$$D(E) = \frac{1}{\pi \hbar v_F}, \quad (1)$$

where  $v_F$  is the Fermi velocity,  $E$  is the energy of the electron,  $E_D$  is the Dirac point, and  $k$  is the momentum of the electron. The spin degree of freedom is taken into account in Eq. (1). The spin of the electrons in the topologically protected edge state is locked to the momentum. We will consider here only the high symmetry zigzag and armchair orientations. The Fermi velocity of the topologically protected helical edge state is not constant, but edge-termination dependent. The dependence of the Fermi velocity on the edge termination can best be understood by considering the projection of the two-dimensional surface reciprocal unit cell in the direction of the edge; see Fig. 3(a). In the case of a zigzag edge, the Fermi velocity is given by [1]

$$v_{F,zz} = \frac{\Delta_{SO}}{\hbar \frac{2\pi}{3a}} = \frac{3\Delta_{SO}a}{h}, \quad (2)$$

where  $\Delta_{SO}$  is the spin-orbit gap and  $a$  is the lattice constant of germanene. For a projection in the armchair direction, different from the zigzag direction, the  $K$  and  $K'$  points collapse onto the  $\Gamma$  point resulting in a Fermi velocity that becomes equal to the Fermi velocity in the interior of the material [see Fig. 3(b)],

$$v_{F,AC} = v_{F,bulk}. \quad (3)$$

To obtain an idea of the values of the zigzag and armchair Fermi velocities we use the experimentally and theoretically available data of germanene ( $\Delta_{SO} = 24\text{--}100$  meV [24,39],  $a = 0.42$  nm [27], and  $v_{F,bulk} = 9 \times 10^5$  m/s [40,41]). We estimate the Fermi velocity of a zigzag edge to be of the order of  $10^4$  m/s, whereas the Fermi velocity of an armchair edge is estimated to be equal to the bulk Fermi velocity. Based on this simple analysis it is immediately clear that the density of

states, which scales as  $v_F^{-1}$ , of a zigzag edge is much higher than the density of states of an armchair edge.

Scanning tunneling spectroscopy is often used to measure the density of states. For small sample biases, the differential conductivity ( $dI/dV$ ) is approximately proportional to the density of states [42,43]. As we will show below, a more detailed analysis reveals that in the case of a single dispersing state, much more information can be extracted from  $dI/dV$  spectra. In our case, the exact shape of the peak in the differential conductivity near the Dirac point allows us to obtain a good estimate for the Fermi velocity of the topologically protected edge state.

We will first derive an expression for  $dI/dV$  in our specific case. The tunnel current is given by

$$I(z, V) = \int_0^{E=eV} D_t(E - eV)D(E)e^{-2\kappa(E)z} dE \\ \approx D_t(0)D(eV)e^{-2\kappa(eV)z} eV, \quad (4)$$

where  $z$  is the tip-substrate distance,  $\kappa$  is the inverse decay length, and  $D_t(E)$  and  $D_s(E)$  are the density of states of the tip and the edge state, respectively. The density of states of the edge state is given by Eq. (1) and the density of states of the metallic scanning tunneling microscopy tip is assumed to be constant (see the Supplemental Material [38]). The inverse decay length is given by [42,43]

$$\kappa(E) = \frac{\sqrt{2m}}{\hbar} \sqrt{\phi + \frac{eV}{2} - E + \frac{\hbar^2 k_{\parallel}^2}{2m}}, \quad (5)$$

where  $\phi = (\phi_s + \phi_t)/2$  is the average work function of tip and substrate and  $k_{\parallel}$  is the parallel momentum of the electronic state of the substrate from or to which tunneling occurs. The largest contribution to the tunnel current usually comes from the electronic states with zero parallel momentum, i.e., the electronic states at the  $\Gamma$  point. If, however, no electronic states are available at the  $\Gamma$  point, the tunnel current will come from electronic states with a nonzero parallel momentum that are closest to the  $\Gamma$  point [42,43]. The inverse decay length  $\kappa(V)$  can be measured via  $dI(V)/dV$  or  $dI(z)/dz$  scanning tunneling spectroscopy [40,42–44]. The inverse dispersion relation, i.e.,  $k_{\parallel}(E)$ , can be obtained from Eq. (5) provided that there is only one energy band (or two bands if the spin degeneracy is taken into account) in the energy window of interest. In our specific case the parallel momentum is one-dimensional and therefore the dispersion relation  $E(k_{\parallel})$  can immediately be obtained by inverting  $k_{\parallel}(E)$  (see the Supplemental Material [38]).

We insert Eq. (1) into Eq. (4) and take the derivative of the current,  $I(z, V)$ , to  $V$ ,

$$\frac{dI(z, V)}{dV} \approx \frac{C}{\pi \hbar v_F} e^{-2\kappa(eV)z}, \quad (6)$$

where  $C$  is a constant. The inverse decay length is given by

$$\kappa(eV) = \frac{\sqrt{2m}}{\hbar} \sqrt{\phi - \frac{e|V|}{2} + \frac{\hbar^2 k_{\parallel}^2}{2m}} \\ = \kappa_0 \sqrt{1 - \frac{e|V|}{2\phi} + \frac{(eV - eV_D)^2}{2mv_F^2\phi}}, \quad (7)$$

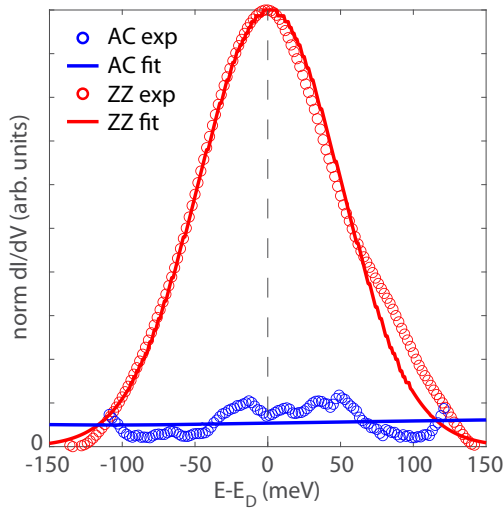


FIG. 4. Differential conductivity of a zigzag and armchair edge versus sample bias (red and blue points). A fit using Eq. (6) with  $v_F = 2.3 \times 10^4$  m/s for the zigzag edge and  $v_F = 5 \times 10^5$  m/s for the armchair edge. Thermal and instrumental broadening are included in the fit (see the Supplemental Material [38]).

where  $\kappa_0 = \frac{\sqrt{2m\phi}}{\hbar}$ . Please note that (i) the largest contribution to the tunnel current comes from electrons that encounter the lowest tunnel barrier, i.e., the electrons with an energy  $E = eV$ , and (ii) the application of a bias voltage  $V$  lowers the effective barrier height by  $-e|V|/2$  (here we take into account that  $V$  can be positive as well as negative).

Owing to their low formation energies, zigzag and armchair edges are the most abundant edge terminations of a honeycomb lattice. The formation energy can be obtained by counting the number of broken bonds per unit length  $a$ . This simple broken bond counting method reveals that the formation energy of an armchair edge is a factor  $\frac{2}{\sqrt{3}}$  higher than the formation energy of a zigzag edge and therefore the zigzag edge termination is the most abundant edge termination. Any germanene edge is basically composed of zigzag and armchair terminated segments.

In Fig. 4 we show the differential conductivity versus sample bias curves recorded at a zigzag and armchair edge. The differential conductivity is recorded at 77 K with a lock-in technique using a modulation voltage of 20 mV, which results in a broadening of the peak. In the Supplemental Material [38]

we provide more information on the thermal and instrumental broadening functions [45–48]. Equation (6) is convoluted with the thermal and instrumental broadening functions and subsequently fitted to the measured  $\frac{dl(V)}{dV}$  curves; see Fig. 4. The fitting results in Fermi velocity of  $(2.3 \pm 0.2) \times 10^4$  m/s for the zigzag edge.

The density of states of an armchair edge is too low for a proper fitting procedure. After subtracting the same background for the zigzag and armchair edges, we find that the density of states of an armchair edge at the Dirac point is a factor of  $\sim 20$  lower than the density of states of a zigzag edge at the Dirac point. The density of states is proportional to  $v_F^{-1}$  and therefore the Fermi velocity of an armchair edge is in the range  $(5 \pm 2) \times 10^5$  m/s, which is slightly lower than the experimentally available data for the bulk Fermi velocity of germanene [40,41].

Finally, in the Supplemental Material [38] we show that the dispersion relation of the zigzag edge can be extracted from the peak shape of the edge state. As assumed earlier, the dispersion relation of the zigzag terminated topological edge state of germanene is indeed quite linear in a large portion of the topological gap, but at the band edges the dispersion relation flattens out a bit.

#### IV. CONCLUSIONS

In conclusion, we have scrutinized the local density of states and dispersion of the zigzag and armchair terminated topological edge state of germanene. We found that the Fermi velocity depends on the termination of the edge. The Fermi velocity is  $(2.3 \pm 0.2) \times 10^4$  m/s at a zigzag edge and  $(5 \pm 2) \times 10^5$  m/s at an armchair edge. Using the Fermi velocity of a zigzag edge, we extract a topological gap of  $75 \pm 10$  meV, which is in good agreement with available experimental data.

#### ACKNOWLEDGEMENTS

H.J.W.Z., D.J.K., and P.B. acknowledge NWO (OCENW.M20.232 and NWO VENI) for financial support. H.J.W.Z. acknowledges the research program “Materials for the Quantum Age” (QuMat) for financial support. This program (Registration No. 024.005.006) is part of the Gravitation program financed by the Dutch Ministry of Education, Culture and Science (OCW).

[1] C. L. Kane and E. J. Mele, Quantum spin Hall effect in graphene, *Phys. Rev. Lett.* **95**, 226801 (2005).  
 [2] C. L. Kane and E. J. Mele,  $Z_2$  topological order and the quantum spin Hall effect, *Phys. Rev. Lett.* **95**, 146802 (2005).  
 [3] B. A. Bernevig, T. L. Hughes, and S.-C. Chang, Quantum spin Hall effect and topological phase transition in HgTe quantum wells, *Science* **314**, 1757 (2006).  
 [4] B. A. Bernevig and S.-C. Chang, Quantum spin Hall effect, *Phys. Rev. Lett.* **96**, 106802 (2006).

[5] M. König, S. Wiedmann, C. Brüne, A. Roth, H. Buhmann, L. W. Molenkamp, X.-L. Qi, and S.-C. Zhang, Quantum spin Hall insulator state in HgTe quantum wells, *Science* **318**, 766 (2007).  
 [6] M. Z. Hasan and C. L. Kane, Topological insulators, *Rev. Mod. Phys.* **82**, 3045 (2010).  
 [7] L. Fu and C. L. Kane, Topological insulators with inversion symmetry, *Phys. Rev. B* **76**, 045302 (2007).  
 [8] D. Hsieh, D. Qian, L. Wray, Y. Xia, Y. S. Hor, R. J. Cava, and M. Z. Hasan, A topological Dirac insulator in a quantum spin Hall phase, *Nature* **452**, 970 (2008).



- [9] J. E. Moore and L. Balents, Topological invariants of time-reversal-invariant band structures, *Phys. Rev. B* **75**, 121306(R) (2007).
- [10] M. Ezawa, Quantized conductance and field-effect topological quantum transistor in silicene nanoribbons, *Appl. Phys. Lett.* **102**, 172103 (2013).
- [11] H. Zhu, C. A. Richter, E. Zhao, J. E. Bonevich, W. A. Kimes, H.-J. Jang, H. Yuan, H. Li, A. Arab, O. Kirillov, J. E. Maslar, D. E. Ioannou, and Q. Li, Topological insulator  $\text{Bi}_2\text{Se}_3$  nanowire high performance field-effect transistors, *Sci. Rep.* **3**, 1757 (2013).
- [12] M. J. Gilbert, Topological electronics, *Commun. Phys.* **4**, 70 (2021).
- [13] S. Das Sarma, M. Freedman, and C. Nayak, Majorana zero modes and topological quantum computation, *NPJ Quantum Inf.* **1**, 15001 (2015).
- [14] X. Qian, J. Liu, L. Fu, and J. Li, Quantum spin Hall effect in two-dimensional transition metal dichalcogenides, *Science* **346**, 1344 (2014).
- [15] Z.-Y. Jia, Y.-H. Song, X.-B. Li, K. Ran, P. Lu, H.-J. Zheng, X.-Y. Zhu, Z.-Q. Shi, J. Sun, J. Wen, D. Xing, and S.-C. Li, Direct visualization of a two-dimensional topological insulator in the single-layer  $1T'-\text{WTe}_2$ , *Phys. Rev. B* **96**, 041108(R) (2017).
- [16] A. Roth, C. Brüne, H. Buhmann, L. W. Molenkamp, J. Maciejko, X.-L. Qi, and S.-C. Zhang, Nonlocal transport in the quantum spin Hall state, *Science* **325**, 294 (2009).
- [17] T. Li, P. Wang, H. Fu, L. Du, K. A. Schreiber, X. Mu, X. Liu, G. Sullivan, G. A. Csáthy, X. Lin, and R.-R. Du, Observation of a helical luttinger liquid in  $\text{InAs}/\text{GaSb}$  quantum spin Hall edges, *Phys. Rev. Lett.* **115**, 136804 (2015).
- [18] I. Knez, R.-R. Du, and G. Sullivan, Evidence for helical edge modes in inverted  $\text{InAs}/\text{GaSb}$  Quantum Wells, *Phys. Rev. Lett.* **107**, 136603 (2011).
- [19] S. Wu, V. Fatemi, Q. D. Gibson, K. Watanabe, T. Taniguchi, R. J. Cava, and P. Jarillo-Herrera, Observation of the quantum spin Hall effect up to 100 Kelvin in a monolayer crystal, *Science* **359**, 76 (2018).
- [20] S. Tang *et al.*, Quantum spin Hall state in monolayer  $1T'-\text{WTe}_2$ , *Nat. Phys.* **13**, 683 (2017).
- [21] Z. Fei, T. Palomaki, S. Wu, W. Zhao, X. Cai, B. Sun, P. Nguyen, J. Finney, X. Xu, and D. H. Cobden, Edge conduction in monolayer  $\text{WTe}_2$ , *Nat. Phys.* **13**, 677 (2017).
- [22] J. L. Collins *et al.*, Electric-field-tuned topological phase transition in ultrathin  $\text{Na}_3\text{Bi}$ , *Nature (London)* **564**, 390 (2018).
- [23] F. Reis, G. Li, M. Bauernfeind, S. Glass, W. Hanke, R. Thomale, J. Schäfer, and R. Claessen, Bismuthene on a SiC substrate: A candidate for a high-temperature quantum spin Hall material, *Science* **357**, 287 (2017).
- [24] P. Bampoulis, C. Castenmiller, D. J. Klaassen, J. van Mil, Y. Liu, C.-C. Liu, Y. Yao, M. Ezawa, A. N. Rudenko, and H. J. W. Zandvliet, Quantum spin Hall states and topological phase transition in germanene, *Phys. Rev. Lett.* **130**, 196401 (2023).
- [25] J. A. Sobota, Y. He, and Z.-X. Shen, Angle-resolved photoemission studies of quantum materials, *Rev. Mod. Phys.* **93**, 025006 (2021), and references therein.
- [26] N. Avraham, J. Reiner, A. Kumar-Nayak, N. Morali, R. Batabyal, B. Yan, and H. Beidenkopf, Quasiparticle interference studies of quantum materials, *Adv. Mater.* **30**, 1707628 (2018), and references therein.
- [27] P. Bampoulis, L. Zhang, A. Safaei, R. van Gastel, B. Poelsema, and H. J. W. Zandvliet, Germanene termination of  $\text{Ge}_2\text{Pt}$  crystals on  $\text{Ge}(110)$ , *J. Phys.: Condens. Matter* **26**, 442001 (2014).
- [28] A. Acun, L. Zhang, P. Bampoulis, M. Farmanbar, M. Lingenfelder, A. van Houselt, A. N. Rudenko, G. Brocks, B. Poelsema, M. I. Katsnelson, and H. J. W. Zandvliet, Germanene: The germanium analogue of graphene, *J. Phys.: Condens. Matter* **27**, 443002 (2015).
- [29] L. Zhang, P. Bampoulis, A. N. Rudenko, Q. Yao, A. van Houselt, B. Poelsema, M. I. Katsnelson, and H. J. W. Zandvliet, Structural and electronic properties of Germanene on  $\text{MoS}_2$ , *Phys. Rev. Lett.* **116**, 256804 (2016).
- [30] F. Bechstedt, P. Gori, and O. Pulci, Beyond graphene: Clean, hydrogenated and halogenated silicene, germanene, stanene, and plumbene, *Prog. Surf. Sci.* **96**, 100615 (2021).
- [31] S. Cahangirov, M. Topsakal, E. Aktürk, H. Şahin, and S. Ciraci, Two- and one-dimensional honeycomb structures of silicon and germanium, *Phys. Rev. Lett.* **102**, 236804 (2009).
- [32] J. Gou, Q. Zhong, S. Sheng, W. Li, P. Cheng, H. Li, L. Chen, and K. Wu, Strained monolayer germanene with  $1 \times 1$  lattice on  $\text{Sb}(111)$ , *2D Mater.* **3**, 045005 (2016).
- [33] Z. Qin, J. Pan, S. Lu, Y. Shao, Y. Wang, S. Du, H.-J. Gao, and G. Cao, Direct evidence of dirac signature in bilayer germanene islands on  $\text{Cu}(111)$ , *Adv. Mater.* **29**, 1606046 (2017).
- [34] Z. Zhang, B. Poelsema, H. J. W. Zandvliet, and A. van Houselt, A microscopic study of the spinodal decomposition of supported eutectic droplets during cooling:  $\text{PtGe}/\text{Ge}\{110\}$ , *J. Phys. Chem. C* **126**, 11285 (2022).
- [35] B. Poelsema, Z. Zhang, J. S. Solomon, H. J. W. Zandvliet, and A. van Houselt, Shining new light on the motion of eutectic droplets across surfaces: A PEEM study of  $\text{PtGe}$  on  $\text{Ge}(110)$ , *Phys. Rev. Mater.* **5**, 125602 (2021).
- [36] Z. Zhang, B. Poelsema, H. J. W. Zandvliet, and A. van Houselt, Detailed characterization of supported eutectic droplets using photoemission electron microscopy, *Phys. Rev. Mater.* **5**, 105601 (2021).
- [37] B. Poelsema, Z. Zhang, H. J. W. Zandvliet, and A. van Houselt, Pre-solidification governs thermal gradient driven propagation of eutectic droplets above  $T_C$ :  $\text{Ge-Pt}/\text{Ge}\{110\}$ , *Phys. Rev. Lett.* **131**, 106201 (2023).
- [38] See Supplemental Material at <http://link.aps.org/supplemental/10.1103/PhysRevB.109.115419> for an additional data set of the differential conductivity of a zigzag edge and the interior of germanene recorded on another sample and with another tip. We also show the offsets of the  $dI/dV$  curves displayed in Fig. 2(c) and provide information on the scanning tunneling microscopy tip preparation procedure, the thermal and instrumental broadening function, and the background subtraction and fitting procedure.
- [39] C.-C. Liu, W. Feng, and Y. Yao, Quantum spin Hall effect in silicene and two-dimensional germanium, *Phys. Rev. Lett.* **107**, 076802 (2011).
- [40] H. J. W. Zandvliet, Q. Yao, L. Zhang, P. Bampoulis, and Z. Jiao, Scanning tunneling spectroscopy of two-dimensional Dirac materials on substrates with a band gap, *Phys. Rev. B* **106**, 085423 (2022).
- [41] M. E. Davila and G. Le Lay, Few layer epitaxial germanene: A novel two-dimensional Dirac material, *Sci. Rep.* **6**, 20714 (2016).

- [42] J. A. Stroscio, R. M. Feenstra, and A. Fein, Electronic-structure of the Si(111) $2 \times 1$  surface by scanning tunneling microscopy, *Phys. Rev. Lett.* **57**, 2579 (1986).
- [43] R. M. Feenstra, J. A. Stroscio, and A. Fein, Tunneling spectroscopy of the Si(111) $2 \times 1$  surface, *Surf. Sci.* **181**, 295 (1987).
- [44] Z. Jiao and H. J. W. Zandvliet, Determination of the Fermi velocity of graphene on MoS<sub>2</sub> using dual mode scanning tunneling spectroscopy, *Appl. Phys. Lett.* **118**, 163103 (2021).
- [45] J. Kröger, L. Limot, H. Jensen, R. Berndt, S. Crampin, and E. Pehlke, Surface state electron dynamics of clean and adsorbate-covered metal surfaces studied with the scanning tunnelling microscope, *Prog. Surf. Sci.* **80**, 26 (2005).
- [46] M. Gruber, A. Weismann, and R. Berndt, The Kondo resonance line shape in scanning tunnelling spectroscopy: Instrumental aspects, *J. Phys.: Condens. Matter* **30**, 424001 (2018).
- [47] B. Borca, C. Castenmiller, M. Tsvetanova, K. Sotthewes, A. N. Rudenko, and H. J. W. Zandvliet, Image potential states of germanene, *2D Mater.* **7**, 035021 (2020).
- [48] L. Matthes and F. Bechstedt, Influence of edge and field effects on topological states of germanene nanoribbons from self-consistent calculations, *Phys. Rev. B* **90**, 165431 (2014).